

Parity-dependent reentrant topology in a Su–Schrieffer–Heeger chain with power-law quasiperiodic modulation

Yusheng Niu^a, Hui Liu^{b,*}, Zhihao Xu^{b,*}

^a*Sanli Honors College, School of Physics and Electronics Engineering, Shanxi University, Taiyuan 030006, China*

^b*Institute of Theoretical Physics and State Key Laboratory of Quantum Optics Technologies and Devices, Shanxi University, Taiyuan 030006, China*

Abstract

We investigate reentrant topological transitions in a one-dimensional Su–Schrieffer–Heeger chain with power-law quasiperiodically modulated intra-cell hopping. The modulation is characterized by a positive integer exponent n and a tunable parameter β , which continuously interpolates between the smooth power-law quasiperiodic limit and a sign-function limit that becomes square-wave-like for odd n and uniform for even n . By combining analytical calculations of the zero-mode inverse localization length with numerical evaluations of a real-space topological indicator, we determine the topological phase diagrams in the $\beta \rightarrow 0$, $\beta \rightarrow \infty$, and finite- β regimes. We show that deterministic quasiperiodic modulation can induce TAI-like reentrant topological phases within finite parameter windows. The formation of these phases depends crucially on the parity of n : for positive modulation strength, odd-power modulations can induce reentrant topology from the clean trivial regime $|t_1| > 1$, whereas even-power modulations allow such reentrance only from the negative clean trivial regime $t_1 < -1$. Exact analytical expressions for the zero-mode inverse localization length are obtained for $n = 1, 2, 3, 4$, yielding explicit or implicit transition conditions. The finite- β results demonstrate that the parity-dependent structure remains robust throughout the interpolation between the two limiting cases. This parity effect originates from

*Corresponding authors.

Email addresses: liuhui99@sxu.edu.cn (Hui Liu), xuzhihao@sxu.edu.cn (Zhihao Xu)

whether the modulation preserves or removes the sign structure of $\cos x$. We further propose an electrical-circuit implementation and discuss experimentally accessible signatures of the reentrant trivial–topological–trivial transition.

Keywords: Su–Schrieffer–Heeger model, quasiperiodic modulation, reentrant topology, zero-mode inverse localization length, topological Anderson-like transition

1. Introduction

Topological phases of matter have attracted sustained interest because of their robust boundary states and unconventional transport properties [1–8]. In one-dimensional systems, the Su–Schrieffer–Heeger (SSH) model serves as a paradigmatic platform for studying chiral-symmetry-protected topological phases [7, 9–12]. In its topological regime, the SSH chain supports zero-energy edge states under open boundary conditions, and its phase transition can be characterized by bulk topological invariants [2, 13–15] as well as by the localization properties of zero modes [13–15].

Disorder and aperiodic modulations can significantly modify the topological properties of low-dimensional systems [7, 16–22]. While disorder generally tends to localize quantum states [23, 24], it may also induce nontrivial topological phases, leading to the so-called topological Anderson insulator (TAI) [12–15, 25–49]. Here the term TAI is used in a broader sense, referring also to reentrant topological phases induced by deterministic quasiperiodic modulations [12, 13, 22], in analogy with the disorder-driven TAI originally proposed for random systems [27, 28, 34, 35, 37]. We emphasize that, since the modulation considered in this work is deterministic rather than random, the term “TAI” should be understood as a topological Anderson-like phase in a generalized sense. In particular, the essential feature discussed below is the reentrant transition from a clean trivial phase to a nontrivial topological phase induced by a spatial modulation [50, 51], rather than a conventional disorder-driven Anderson mechanism. In parallel, quasiperiodic systems provide an intermediate setting between periodic order and random disorder, and have become an important platform for exploring the interplay among topology [7, 17–22], localization [20, 22, 52–55], and spectral criticality [52, 56, 57]. In recent years, disorder- or quasiperiodicity-driven topological transitions have been extensively investigated in SSH-type lattices and related one-dimensional models [3, 11–14, 58, 59]. However, existing studies

have largely focused on either purely random disorder [27, 28, 34, 35, 37] or simple cosine-type quasiperiodic modulations [12, 13]. The effects of power-law quasiperiodic modulations, especially how the modulation exponent and profile reshape reentrant topological phases, remain much less explored.

Motivated by this issue, we study a generalized SSH chain with a tunable hopping modulation [52, 55], where a control parameter β continuously interpolates between the power-law quasiperiodic limit and a sign-function limit that becomes square-wave-like for odd n and uniform for even n . This unified setting enables us to examine not only the limiting cases but also the continuous evolution of the topological phase diagram between them.

In this work, we combine analytical and numerical methods to investigate the topological phase transitions in this model. The central finding is a clear parity dependence of the phase diagrams on the power exponent n : odd and even exponents lead to qualitatively different transition patterns and distinct mechanisms for the emergence of reentrant topological phases. By analyzing the zero-mode inverse localization length, we obtain exact analytical expressions for $n = 1, 2, 3, 4$, which yield explicit or implicit transition conditions. These analytical results are confirmed by numerical evaluations of the real-space topological indicator [1, 15, 49]. We show that deterministic quasiperiodic modulation can induce TAI-like reentrant topological phases within finite parameter windows. We also propose an electrical-circuit realization of the model, which offers a possible route for experimental verification.

The remainder of this paper is organized as follows. In Section 2, we introduce the model and the topological characterization methods. In Section 3, we present the topological phase diagrams in three parameter regimes ($\beta \rightarrow 0$, $\beta \rightarrow \infty$, and finite β), and consolidate the results into a unified picture of the parity-dependent reentrant topology. In Section 4, we outline an electrical-circuit implementation. Section 5 summarizes the main findings. Analytical details are provided in the Appendices.

2. Model and topological criterion

We consider a one-dimensional SSH chain with $L = 2N$ lattice sites, corresponding to N unit cells, as illustrated in Fig. 1. Each unit cell contains two sublattices, labeled A and B . The red solid lines denote the intracell hopping, whereas the black dashed lines denote the intercell hopping. Within

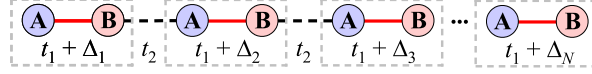


Figure 1: Schematic illustration of the SSH chain with quasiperiodically modulated intracell hopping $\omega_j = t_1 + \Delta_j$ and uniform intercell hopping t_2 .

the tight-binding approximation, the Hamiltonian is given by

$$H = \sum_j \omega_j \left(c_{j,B}^\dagger c_{j,A} + \text{h.c.} \right) + t_2 \sum_j \left(c_{j+1,A}^\dagger c_{j,B} + \text{h.c.} \right), \quad (1)$$

where $\omega_j = t_1 + \Delta_j$ is the intracell hopping amplitude, with t_1 the uniform part and Δ_j the quasiperiodic modulation. The intercell hopping amplitude t_2 is taken as the energy unit, i.e., $t_2 = 1$. Here, $c_{j,A}$ ($c_{j,B}$) and $c_{j,A}^\dagger$ ($c_{j,B}^\dagger$) denote the annihilation and creation operators on sublattice A (B) in the j th unit cell, respectively. The modulation is chosen as

$$\Delta_j = \lambda \frac{\tanh[\beta \cos^n(2\pi\alpha j)]}{\tanh \beta}, \quad (2)$$

where λ denotes the modulation strength and β is a tunable parameter controlling the profile of the modulation. The exponent n is taken to be a positive integer, and $\alpha = (\sqrt{5} - 1)/2$ is taken as the irrational modulation frequency.

This modulation continuously interpolates between different limiting cases. In the limit $\beta \rightarrow 0$, one has $\Delta_j \approx \lambda \cos^n(2\pi\alpha j)$, which corresponds to a power-law quasiperiodic modulation. In the opposite limit $\beta \rightarrow \infty$, the modulation approaches $\Delta_j \approx \lambda \text{sgn}[\cos^n(2\pi\alpha j)]$. For odd n , one has $\text{sgn}[\cos^n x] = \text{sgn}(\cos x)$, so that the modulation becomes square-wave-like. For even n , $\text{sgn}[\cos^n(2\pi\alpha j)] = 1$ for all lattice sites, so that the modulation becomes effectively uniform. In this work, we investigate the topological phase transitions induced by this quasiperiodic modulation in different β regimes.

Because the Hamiltonian in Eq. (1) contains only off-diagonal hopping terms, the model preserves chiral symmetry. For this class of one-dimensional chiral systems, the topological phase boundary can be determined from the zero-energy transfer equation. At zero energy, the eigenvalue equation decouples into two independent recurrence relations on the two sublattices [14]. For the A sublattice, one obtains

$$\psi_{j+1,A} = -\frac{\omega_j}{t_2} \psi_{j,A}, \quad (3)$$

with an analogous relation for the B sublattice. The inverse localization length of the zero-energy mode is determined by the exponential growth or decay rate of the corresponding transfer product [13–15]. We define it as

$$\nu = \left| \lim_{N \rightarrow \infty} \frac{1}{N} \sum_{j=1}^N \ln \left| \frac{t_2}{\omega_j} \right| \right|. \quad (4)$$

Here ν is non-negative by definition. Therefore, it characterizes the localization length of the zero-energy mode and determines the phase boundary through $\nu = 0$ [7, 13–15]. In the following, we use $\nu = 0$ to determine the analytical phase boundaries, while the topological character of each region is identified by the real-space topological indicator.

For chiral SSH-type chains with off-diagonal modulation, a convenient real-space topological indicator is [1, 15, 49]

$$Q = \frac{1}{2} \left[1 - \text{sgn} \left(\prod_j \omega_j^2 - \prod_j t_2^2 \right) \right], \quad (5)$$

where the product runs over all unit cells. Specifically, $Q = 1$ and $Q = 0$ correspond to the topologically nontrivial and trivial phases, respectively. The phase boundary obtained from Q is consistent with the zero-mode condition $\nu = 0$. In the following, we use Q to construct the numerical phase diagrams and $\nu = 0$ to derive the analytical phase boundaries. In the figures, the topologically nontrivial and trivial regions are indicated by purple and gold, respectively.

3. Phase diagrams

Unless otherwise stated, we focus on positive modulation strength $\lambda > 0$ in the phase diagrams. For odd n , the phase diagram is symmetric under $\lambda \rightarrow -\lambda$ because the modulation retains a sign-changing distribution. For even n , changing the sign of λ reverses the direction of the non-negative hopping shift and correspondingly exchanges the roles of the positive- and negative- t_1 trivial regimes.

3.1. $\beta \rightarrow 0$ limit

We first consider the limit $\beta \rightarrow 0$, in which the intracell hopping reduces to $\omega_j = t_1 + \lambda \cos^n(2\pi\alpha j)$. Setting $t_2 = 1$ in Eq. (4), the inverse localization

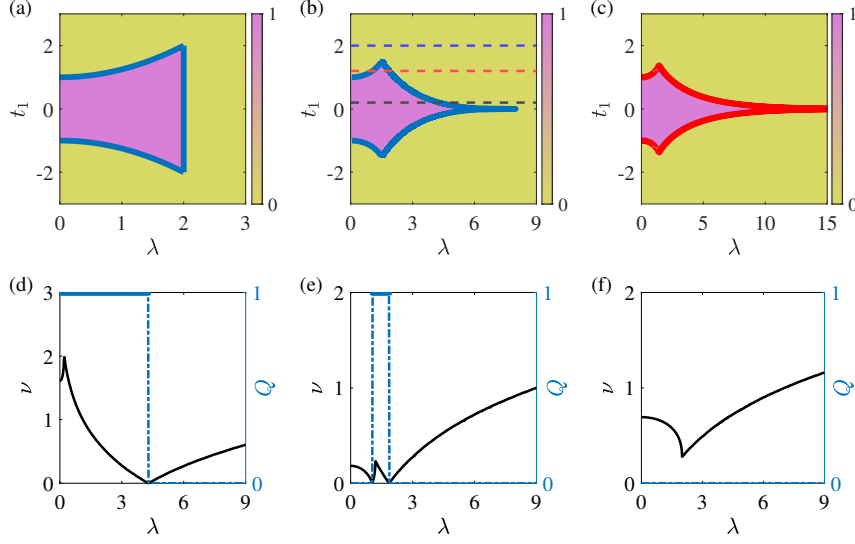


Figure 2: Topological phase diagrams and zero-mode inverse-localization-length analysis in the $\beta \rightarrow 0$ limit for odd n . The colored regions in (a)–(c) are obtained from the numerical topological indicator Q , while the solid lines denote the phase boundaries determined from the criterion $\nu = 0$. The blue solid lines represent analytical phase boundaries, and the red solid lines denote the boundaries obtained from numerical integration of Eq. (7). (a) $n = 1$. (b) $n = 3$, where the horizontal dashed lines indicate $t_1 = 0.2, 1.2$, and 2 . (c) $n = 5$. (d) $n = 3, t_1 = 0.2$. (e) $n = 3, t_1 = 1.2$. (f) $n = 3, t_1 = 2$. Here $L = 1000$.

length of the zero-energy mode can be written as

$$\nu = \left| \lim_{N \rightarrow \infty} \frac{1}{N} \sum_{j=1}^N \ln |t_1 + \lambda \cos^n[2\pi\alpha(j + j_0)]| \right|, \quad (6)$$

where j_0 denotes an arbitrary initial site index. Because α is irrational, the sequence $2\pi\alpha(j + j_0)$ is equidistributed modulo 2π in the thermodynamic limit. The spatial average in Eq. (6) can therefore be replaced by an integral over one period [3, 58], yielding

$$\nu = \left| \frac{1}{2\pi} \int_0^{2\pi} \ln |t_1 + \lambda \cos^n x| dx \right|. \quad (7)$$

The topological phase boundary is determined by the zero-mode delocalization condition $\nu = 0$.

For odd n , Figs. 2(a)–2(c) show the phase diagrams in the (t_1, λ) plane for $n = 1, 3$, and 5 , respectively. In all odd- n cases considered here, the system can enter a TAI-like reentrant topological phase within a finite interval of modulation strength for an appropriate range of t_1 .

For $n = 1$, the analytical phase boundaries derived in Refs. [13, 14] are

$$\begin{cases} |t_1| = \frac{\lambda^2}{4} + 1, & |t_1/\lambda| > 1, \quad |\lambda| \leq 2, \\ |\lambda| = 2, & 0 < |t_1/\lambda| < 1. \end{cases} \quad (8)$$

These analytical boundaries, plotted as blue solid curves in Fig. 2(a), agree very well with the numerical phase diagram. The two branches of Eq. (8) merge at the terminal point $(\lambda, |t_1|) = (2, 2)$, beyond which the first branch ceases to exist. In particular, within the interval $1 < |t_1| < 2$ (where the upper bound is set by this terminal point), the system undergoes a reentrant transition: it is trivial at weak modulation, enters a TAI-like topological phase at intermediate λ , and returns to the trivial phase when λ is further increased.

For $n = 3$, the zero-mode inverse localization length can likewise be evaluated analytically. The detailed derivation is presented in Appendix [Appendix A.1](#), where the integral in Eq. (7) is reduced to an exact analytic expression. The phase boundary then follows from the condition $\nu = 0$ applied to that expression. The resulting analytical boundary is plotted in Fig. 2(b), showing good agreement with the numerical results. In the interval approximately given by $1 < |t_1| \lesssim 1.5$, where the upper bound is obtained from the condition $\nu = 0$ using the exact expression in Appendix [Appendix A.1](#), the system also exhibits a reentrant transition sequence from a trivial phase to a TAI-like reentrant topological phase and then back to the trivial phase as λ increases. Figures 2(d)–2(f) further display ν and Q as functions of λ for representative values of t_1 . For $t_1 = 0.2$, the system undergoes a single topological-to-trivial transition, signaled simultaneously by a jump in Q and the vanishing of ν . For $t_1 = 1.2$, two transition points appear, confirming the emergence of a TAI-like reentrant topological phase. By contrast, for $t_1 = 2$, the system remains trivial for all λ .

The same qualitative behavior persists for higher odd exponents. For example, the phase boundary shown for $n = 5$ in Fig. 2(c) is obtained numerically from the zero-mode inverse-localization-length criterion in Eq. (7), and displays the same reentrant structure. This indicates that the TAI-

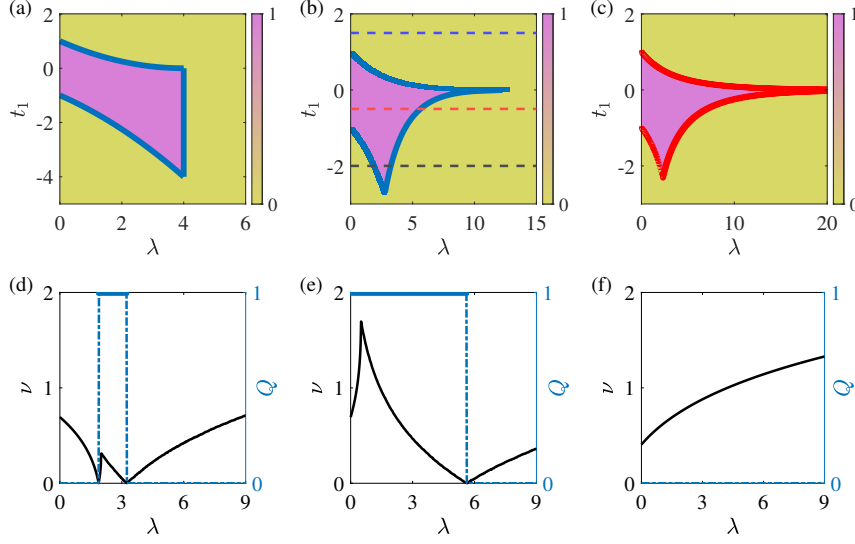


Figure 3: Topological phase diagrams and zero-mode inverse-localization-length analysis in the $\beta \rightarrow 0$ limit for even n . The colored regions in (a)–(c) are obtained from the numerical topological indicator Q , while the solid lines denote the phase boundaries determined from the criterion $\nu = 0$. The blue solid lines represent analytical phase boundaries, and the red solid lines denote the boundaries obtained from numerical integration of Eq. (7). (a) $n = 2$. (b) $n = 4$, where the horizontal dashed lines indicate $t_1 = -2, -0.5$, and 1.5 . (c) $n = 6$. (d) $n = 4, t_1 = -2$. (e) $n = 4, t_1 = -0.5$. (f) $n = 4, t_1 = 1.5$. Here $L = 1000$.

like reentrant topological phase persists for odd $n \geq 3$, suggesting a robust parity-dependent mechanism.

The odd- n results show that the sign-changing nature of the modulation can support a reentrant topological phase within a finite modulation window. More precisely, for positive λ , odd-power modulations can induce a TAI-like reentrant phase from the clean trivial regime $|t_1| > 1$, although the actual existence range and width of this window depend on n . Thus, the condition $|t_1| > 1$ should be understood as the clean trivial regime from which the reentrant phase can be induced, rather than as a sufficient condition for its existence at arbitrary modulation strength.

In contrast to the odd- n case, the even- n phase diagrams shown in Figs. 3(a)–3(c) display a qualitatively different structure for $n = 2, 4$, and 6 . The system again enters a TAI-like reentrant topological phase within a finite interval of λ for suitable t_1 , but the relevant parameter region is now restricted to neg-

ative t_1 . For $n = 2$, analytical evaluation of Eq. (7) yields

$$\nu = \begin{cases} \left| 2 \ln \left| 1 + \sqrt{\lambda/t_1 + 1} \right| + \ln |t_1| - \ln 4 \right|, & \lambda/t_1 > -1, \\ |\ln |\lambda/4||, & \lambda/t_1 < -1, \end{cases} \quad (9)$$

from which the phase boundaries follow as

$$\begin{cases} t_1 = 1 - \frac{\lambda}{2} + \frac{\lambda^2}{16} \quad \text{or} \quad t_1 = -\left(1 + \frac{\lambda}{2} + \frac{\lambda^2}{16}\right), & \lambda/t_1 > -1, \\ |\lambda| = 4, & \lambda/t_1 < -1. \end{cases} \quad (10)$$

The detailed derivation of ν is presented in Appendix [Appendix A.2](#). The structure of Eq. (10) reflects the fact that for $n = 2$ the modulation $\lambda \cos^2 x$ is non-negative for positive λ . Therefore, the modulation shifts the intracell hopping toward larger values. It can reduce the magnitude of a negative trivial hopping with $t_1 < -1$ by partially compensating the negative uniform component, but it cannot reduce a positive trivial hopping with $t_1 > 1$. This asymmetry explains why, for positive λ , the reentrant TAI-like phase is confined to the negative- t_1 side for even n . In terms of the zero-mode criterion, the transition occurs when the inverse localization length ν vanishes, while the topological character of the two sides is identified by the indicator Q . The analytical boundaries shown in Fig. 3(a) agree very well with the numerical phase diagram. In the interval $-4 < t_1 < -1$, the system undergoes a reentrant transition from the trivial phase to a TAI-like reentrant topological phase and finally back to the trivial phase as λ increases. For $n = 4$, the zero-mode inverse localization length can likewise be evaluated analytically, and its exact analytic expression is presented in Appendix [Appendix A.3](#). The corresponding phase boundaries determined from $\nu = 0$ are

$$\begin{cases} \left| 1 + \sqrt{1 + \kappa} \right|^2 \left| 1 + \sqrt{1 - \kappa} \right|^2 |t_1| = 16, & \lambda/t_1 > -1, \\ \left| 1 + \sqrt{1 + \kappa} \right|^2 |\kappa t_1| = 16, & \lambda/t_1 < -1, \end{cases} \quad (11)$$

where $\kappa = (-\lambda/t_1)^{1/2}$. These analytical boundaries, plotted in Fig. 3(b), again agree very well with the numerical results. In the interval $-2.74 < t_1 < -1$ (where the lower bound is determined numerically from the condition $\nu = 0$ using the exact analytic expression for the zero-mode inverse localization length in Appendix [Appendix A.3](#)), the system exhibits the same

reentrant behavior. For higher even exponents such as $n = 6$, the phase boundary shown in Fig. 3(c) is likewise obtained numerically from the zero-mode inverse-localization-length criterion in Eq. (7). The resulting phase diagram further confirms that this behavior remains qualitatively unchanged for higher even exponents, suggesting that the TAI-like reentrant topological phase is a robust feature for even $n \geq 4$. Figures 3(d)–3(f) show representative curves of ν and Q versus λ . For $t_1 = -2$, two transition points are clearly visible, confirming the emergence of a TAI-like reentrant topological phase. For $t_1 = -0.5$, only one transition from the topologically nontrivial phase to the trivial phase is observed. By contrast, for $t_1 = 1.5$ the system remains trivial for all λ .

Having established the phase diagrams in the smooth quasiperiodic limit, we now turn to the opposite extreme and examine how the topological structure changes when the modulation profile approaches its sign-function limit.

3.2. $\beta \rightarrow \infty$ limit

We next consider the opposite limit $\beta \rightarrow \infty$, for which the intracell hopping becomes $\omega_j = t_1 + \lambda \operatorname{sgn}[\cos^n(2\pi\alpha j)]$. The inverse localization length of the zero-energy mode is then given by

$$\nu = \left| \lim_{N \rightarrow \infty} \frac{1}{N} \sum_{j=1}^N \ln |t_1 + \lambda \operatorname{sgn}[\cos^n(2\pi\alpha(j + j_0))]| \right|, \quad (12)$$

where j_0 is an arbitrary initial site index, as in Eq. (6). Using the same argument as in Eq. (7), the inverse localization length can be expressed as

$$\nu = \left| \frac{1}{2\pi} \int_0^{2\pi} \ln |t_1 + \lambda \operatorname{sgn}(\cos^n x)| dx \right|. \quad (13)$$

As in the $\beta \rightarrow 0$ limit, we discuss the odd- and even- n cases separately.

For odd n , one has $\operatorname{sgn}(\cos^n x) = \operatorname{sgn}(\cos x)$, so that the quasiperiodic modulation is reduced to a binary square-wave form with $\Delta_j = \pm\lambda$. Since the two values $\pm\lambda$ occur with equal weight in the thermodynamic limit, Eq. (13) yields the inverse localization length

$$\nu = \frac{1}{2} \left| \ln |t_1^2 - \lambda^2| \right|. \quad (14)$$

The corresponding phase boundaries are determined from $\nu = 0$ as

$$|t_1^2 - \lambda^2| = 1. \quad (15)$$

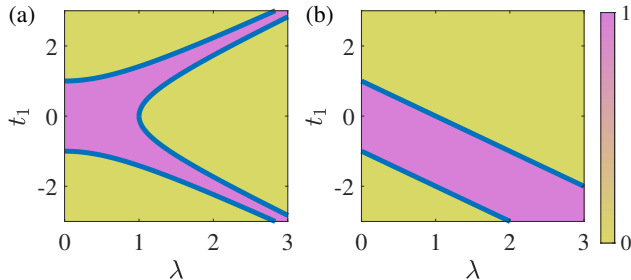


Figure 4: Topological phase diagrams in the $\beta \rightarrow \infty$ limit. The colored regions are obtained from the numerical topological indicator Q , and the blue solid lines denote the analytical phase boundaries determined by $\nu = 0$. (a) Odd n . (b) Even n . Here $L = 1000$.

Figure 4(a) shows the phase diagram in the (t_1, λ) plane for the odd- n case. The analytical boundaries from Eq. (15) are plotted as blue solid curves and agree well with the numerical results. In the interval $|t_1| > 1$, the system exhibits a reentrant transition sequence: it is trivial at weak modulation, enters a TAI-like reentrant topological phase at intermediate λ , and returns to the trivial phase when λ is further increased. Compared with the $\beta \rightarrow 0$ limit, the topological region in the present case extends to progressively larger λ as $|t_1|$ increases, indicating that stronger modulation can still support a topological phase provided that the uniform hopping is tuned simultaneously.

For even n , one has $\text{sgn}(\cos^n x) = 1$, so that all even- n cases reduce to a uniform modulation with $\Delta_j = \lambda$. In this case Eq. (13) simplifies to

$$\nu = |\ln |t_1 + \lambda||, \quad (16)$$

and the phase boundary is determined by

$$|t_1 + \lambda| = 1. \quad (17)$$

It should be emphasized that, in the even- n case, the $\beta \rightarrow \infty$ limit is qualitatively different from a genuine quasiperiodic or disorder-induced TAI mechanism, where the modulation becomes spatially uniform and simply shifts the intracell hopping from t_1 to $t_1 + \lambda$. Therefore, the corresponding reentrant transition in this limiting case should be regarded as a uniform hopping-shift-induced transition rather than a genuine quasiperiodicity-induced topological Anderson mechanism. Nevertheless, this limit is useful as an endpoint of the continuous interpolation controlled by β and highlights the parity-dependent loss of the sign structure for even powers. Figure 4(b) shows the

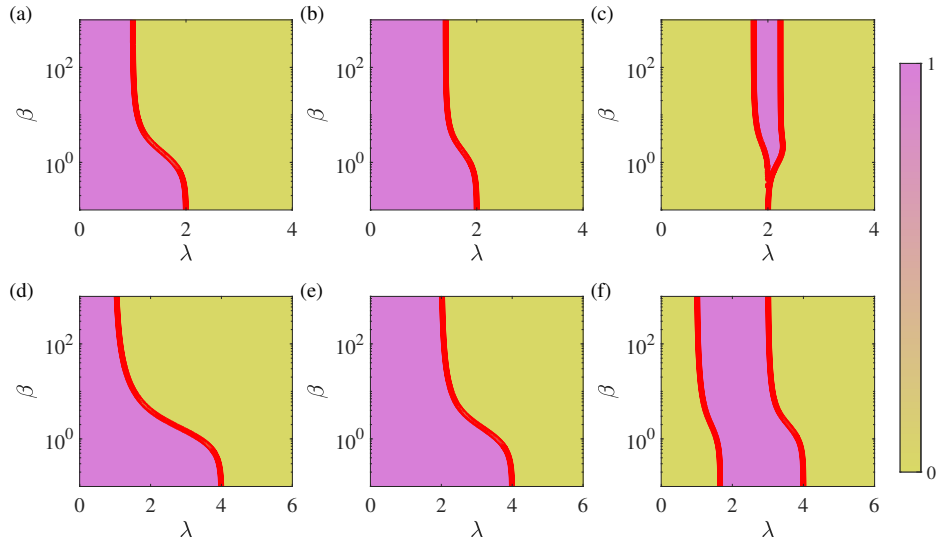


Figure 5: Topological phase diagrams in the (β, λ) plane for continuously varying β . The colored regions are obtained from the numerical topological indicator Q , and the red solid lines denote the phase boundaries determined from the zero-mode condition $\nu(\beta) = 0$. (a)–(c) $n = 1$ with $t_1 = 0, 1,$ and 2 , respectively. (d)–(f) $n = 2$ with $t_1 = 0, -1,$ and -2 , respectively. Here $L = 1000$.

corresponding phase diagram for the even- n case. The analytical boundaries from Eq. (17) are plotted as blue solid lines and are in excellent agreement with the numerical phase boundaries. In the region $t_1 < -1$, the system again undergoes a reentrant transition from a trivial phase to a TAI-like reentrant topological phase and then back to the trivial phase as λ increases. In contrast to the odd- n case, however, the topological region has a constant width, reflecting the fact that the $\beta \rightarrow \infty$ limit for even n corresponds to an effectively uniform modulation rather than a binary aperiodic one.

The two limiting cases thus reveal a clear parity-dependent contrast in the topological phase structure. In the following, we examine whether this contrast persists throughout the continuous interpolation between the two limits.

3.3. Continuously varying β

We now turn to the intermediate regime of finite β , which continuously interpolates between the two analytically tractable limits discussed above.

The central question is whether the parity-dependent topological structure identified in those limits remains robust throughout this interpolation.

For arbitrary positive integer n , the intracell hopping at finite β takes the form

$$\omega_j = t_1 + \lambda \frac{\tanh[\beta \cos^n(2\pi\alpha j)]}{\tanh \beta}. \quad (18)$$

Using the same equidistribution argument as in Eq. (7), the inverse localization length of the zero-energy mode is

$$\nu(\beta) = \left| \frac{1}{2\pi} \int_0^{2\pi} \ln \left| t_1 + \lambda \frac{\tanh(\beta \cos^n x)}{\tanh \beta} \right| dx \right|. \quad (19)$$

The topological phase boundary is determined implicitly by the zero-mode delocalization condition

$$\nu(\beta) = 0. \quad (20)$$

Although this equation does not generally admit a closed-form solution for finite β , it can be evaluated numerically with high precision and correctly reproduces the analytical phase boundaries in both limiting cases. The topological character of the regions separated by these boundaries is determined from the real-space indicator Q .

Figure 5 summarizes the resulting phase diagrams in the (β, λ) plane, with $n = 1$ and $n = 2$ taken as representative odd- and even- n cases, respectively. For odd n , as shown in Figs. 5(a)–5(c), the three panels correspond to qualitatively distinct clean-limit regimes: $t_1 = 0$ lies in the clean topological phase, $t_1 = 1$ is the clean critical point, and $t_1 = 2$ lies in the clean trivial phase. Only for $t_1 = 2$, which starts from the clean trivial regime $|t_1| > 1$, does a reentrant TAI-like topological window emerge at intermediate modulation strength. For even n , as shown in Figs. 5(d)–5(f), the panels correspond to $t_1 = 0$ (clean topological), $t_1 = -1$ (clean critical), and $t_1 = -2$ (clean trivial on the negative side). A reentrant TAI-like region appears only for $t_1 = -2$, consistent with the even- n mechanism.

These results confirm that the reentrant topological phase persists throughout the continuous variation of β whenever the corresponding modulation window exists. While the precise location and width of the reentrant window evolve smoothly with β , the underlying transition pattern remains unchanged. For positive λ , odd- n modulations can induce reentrant topology from the clean trivial regime $|t_1| > 1$, whereas even- n modulations can do so

only from the negative clean trivial side $t_1 < -1$. Thus, varying β continuously deforms the phase boundary determined by $\nu = 0$ without altering the parity-controlled mechanism of reentrant topology formation.

3.4. Parity effect: a unified picture

The results of Sections 3.1–3.3 reveal a systematic parity dependence of the topological phase structure on the power exponent n that persists across all three parameter regimes. We summarize this parity effect here.

For odd n , the function $\cos^n x$ retains the sign alternation of $\cos x$. Consequently, the $\beta \rightarrow 0$ modulation $\lambda \cos^n(2\pi\alpha j)$ changes sign across the lattice, and the $\beta \rightarrow \infty$ limit reduces to a binary $\pm\lambda$ square wave in which the two values occur with equal weight. This sign-changing profile strongly reshapes the distribution of $|\omega_j|$ and can drive the zero-mode inverse localization length to zero at finite modulation strength. As a result, for positive λ , a TAI-like reentrant topological phase can be induced from the clean trivial regime $|t_1| > 1$ within finite modulation windows. The actual range of t_1 and the width of the window depend on n and β . In the $\beta \rightarrow \infty$ limit, the topological region is bounded by the hyperbola $|t_1^2 - \lambda^2| = 1$: unlike the $\beta \rightarrow 0$ case, the upper boundary of the reentrant window in λ grows without bound as $|t_1| \rightarrow \infty$, so that stronger modulation is required to destroy the topological phase for larger $|t_1|$.

For even n , the function $\cos^n x$ is non-negative, and the sign information of $\cos x$ is removed. For positive λ , the modulation shifts the intracell hopping toward larger values. It can compensate a negative trivial hopping with $t_1 < -1$, but it cannot reduce a positive trivial hopping with $t_1 > 1$. This explains why, for positive λ , the reentrant TAI-like phase is confined to the negative- t_1 side for even n . In the $\beta \rightarrow \infty$ limit, the topological region has a constant width in λ , reflecting the uniform nature of the limiting modulation.

The key distinction between odd and even n is therefore qualitative: it originates from whether the modulation retains or removes the sign structure of $\cos x$, which determines how the modulation reshapes the zero-energy transfer product and hence controls the formation and disappearance of the reentrant topological phase. This difference in sign structure is the fundamental reason why odd and even powers lead to distinct reentrant topology formation mechanisms. More specifically, odd powers allow the effective hopping to alternate in sign across the lattice, whereas even powers merely shift the hopping in a non-negative manner; as a result, the reentrant TAI-like phase for even n can only be induced from the negative- t_1 side. This

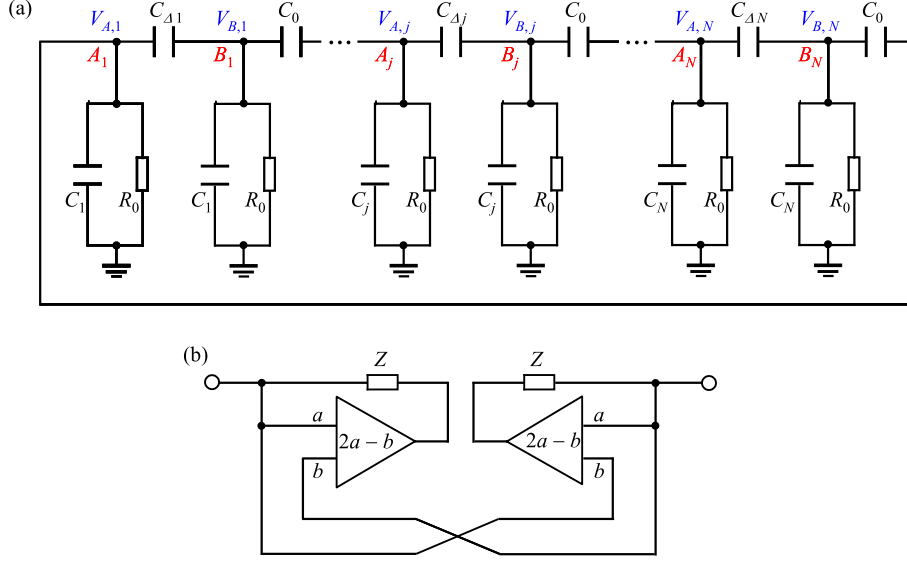


Figure 6: Electrical-circuit implementation of the model. (a) Main circuit under periodic boundary conditions. Adjacent nodes represent the A and B sublattices of the SSH chain. (b) Two-terminal active circuit used to realize an effective negative capacitance. Here Z denotes an arbitrary impedance element.

parity-dependent mechanism is robust throughout the continuous interpolation controlled by β : varying β deforms the location and width of the reentrant window continuously without altering the underlying transition mechanism.

4. Electrical-circuit implementation

The reentrant topological phase predicted above can be implemented and detected in an electrical-circuit platform. To this end, we propose the circuit shown in Fig. 6, which realizes the Hamiltonian in Eq. (1). As illustrated in Fig. 6(a), adjacent nodes in the AC circuit chain represent the A and B sublattices of the SSH model. The capacitors $C_{\Delta j}$ and C_0 simulate the intracell and intercell hoppings, respectively. Here $C_{\Delta j}$ corresponds to the full intracell hopping amplitude $\omega_j = t_1 + \Delta_j$, while C_0 represents the uniform intercell hopping. The node voltages $V_{A,j}$ and $V_{B,j}$ correspond to the wave-function amplitudes on the two sublattices. In addition, the grounded capacitor C_j is introduced to balance the on-site terms, while the resistor R_0

is included to protect the circuit. In the present implementation, C_0 serves as the reference capacitance corresponding to the intercell hopping scale.

When an effective negative capacitance is required for $C_{\Delta j}$ or C_j , it can be realized by the two-terminal active circuit shown in Fig. 6(b), which consists of two capacitors and two operational amplifiers [60]. For an AC driving frequency Ω , the Hamiltonian in Eq. (1) is mapped onto the circuit Laplacian $\mathcal{J}(\Omega)$, which relates the input-current vector $I(\Omega)$ to the node-voltage vector $V(\Omega)$ through

$$I(\Omega) = \mathcal{J}(\Omega)V(\Omega). \quad (21)$$

Applying Kirchhoff's current law to the bulk and boundary nodes yields

$$\begin{aligned} I_{A,j} &= i\Omega C_0 V_{B,j-1} + i\Omega C_{\Delta j} V_{B,j} - i\Omega \left(C_0 + C_{\Delta j} + \frac{1}{i\Omega R_0} + C_j \right) V_{A,j}, \\ I_{B,j} &= i\Omega C_{\Delta j} V_{A,j} + i\Omega C_0 V_{A,j+1} - i\Omega \left(C_0 + C_{\Delta j} + \frac{1}{i\Omega R_0} + C_j \right) V_{B,j}, \end{aligned} \quad (22)$$

while the boundary cells under periodic boundary conditions obey

$$\begin{aligned} I_{A,1} &= i\Omega C_0 V_{B,N} + i\Omega C_{\Delta 1} V_{B,1} - i\Omega \left(C_0 + C_{\Delta 1} + \frac{1}{i\Omega R_0} + C_1 \right) V_{A,1}, \\ I_{B,N} &= i\Omega C_{\Delta N} V_{A,N} + i\Omega C_0 V_{A,1} - i\Omega \left(C_0 + C_{\Delta N} + \frac{1}{i\Omega R_0} + C_N \right) V_{B,N}. \end{aligned} \quad (23)$$

Here $I_{\sigma,j}$ and $V_{\sigma,j}$ denote the current and voltage at sublattice $\sigma \in \{A, B\}$ in the j th unit cell, respectively. By choosing $C_{\Delta j} = \omega_j C_0 = (t_1 + \Delta_j)C_0$, and $C_j = -(C_0 + C_{\Delta j})$, the circuit Laplacian in the basis $(V_{A,1}, V_{B,1}, V_{A,2}, V_{B,2}, \dots, V_{A,N}, V_{B,N})^T$ takes the form

$$\mathcal{J}(\Omega) = i\Omega \mathcal{M} - \frac{1}{R_0} \mathcal{I}, \quad (24)$$

where \mathcal{I} is the $2N \times 2N$ identity matrix, and the nonzero elements of \mathcal{M} are given by

$$\begin{aligned} \mathcal{M}_{2j-1,2j} &= \mathcal{M}_{2j,2j-1} = C_{\Delta j} & (j = 1, \dots, N), \\ \mathcal{M}_{2j,2j+1} &= \mathcal{M}_{2j+1,2j} = C_0 & (j = 1, \dots, N-1), \end{aligned}$$

together with the periodic boundary terms $\mathcal{M}_{2N,1} = \mathcal{M}_{1,2N} = C_0$, while all remaining matrix elements vanish. The circuit Laplacian therefore reproduces the target SSH Hamiltonian up to the overall prefactor $i\Omega C_0$ and the uniform diagonal shift $-R_0^{-1}\mathcal{I}$.

While Fig. 6(a) illustrates the periodic-boundary implementation used to reproduce the bulk Hamiltonian, the detection of topological boundary modes can be carried out in the corresponding open-boundary circuit obtained by removing the end-to-end connection. In this case, the spatial distribution of the eigenstates can be probed directly through voltage measurements at the circuit nodes [60].

To experimentally detect the reentrant topological phase, one may measure the node-voltage distribution and the two-point impedance under open boundary conditions. In the topologically nontrivial regime, the circuit Laplacian supports boundary-localized eigenvectors corresponding to the SSH edge modes. When an AC current is injected near the boundary, the voltage response is therefore strongly concentrated near the edge nodes in the low-loss regime. By contrast, such boundary-localized voltage profiles are absent in the trivial regime. A complementary probe is provided by the two-point impedance between boundary nodes. The impedance matrix is determined by the inverse of the circuit Laplacian and is therefore sensitive to eigenmodes with small admittance. In the topological regime, the boundary-localized mode produces an enhanced edge response compared with the trivial regime. Thus, by varying the modulation strength λ , the appearance and disappearance of an enhanced boundary response can serve as an experimental signature of the reentrant trivial–topological–trivial transition predicted in this model. In addition, one may inject an AC current from one boundary node and measure the voltage response at the opposite boundary, thereby obtaining a two-terminal probe of the reentrant topological phase. These measurements are well within the capabilities of existing topoelectrical-circuit platforms [60].

5. Conclusion

In conclusion, we have established the topological phase diagrams of a one-dimensional SSH chain with power-law quasiperiodic modulation, covering the smooth quasiperiodic limit ($\beta \rightarrow 0$), the sign-function limit ($\beta \rightarrow \infty$), which is square-wave-like for odd n and uniform for even n , and the full continuous interpolation between them. The real-space topological indicator Q and the zero-mode inverse-localization-length criterion $\nu = 0$ are in excellent agreement throughout the parameter space, confirming that deterministic quasiperiodic modulation can induce TAI-like reentrant topological phases within finite parameter windows. The central result is that the structure

of these phase diagrams depends fundamentally on the parity of the power exponent n .

As detailed in Section 3.4, this parity effect originates from whether the modulation retains the sign structure of $\cos x$. Odd powers preserve the sign alternation and therefore produce phase diagrams qualitatively different from those for even powers, which remove the sign information entirely. This distinction persists across all three parameter regimes and is captured analytically by the zero-mode inverse-localization-length criterion, which continues to provide accurate phase boundaries throughout the continuous interpolation between the two limiting cases. The proposed electrical-circuit implementation offers a direct experimental route to observe the reentrant trivial–topological–trivial transition via boundary voltage and impedance measurements. These results clarify how the interplay between quasiperiodicity and modulation parity reshapes reentrant topological transitions in one-dimensional chiral systems, and suggest that the parity-dependent mechanism may extend to higher-dimensional generalizations of chiral-symmetric models.

Appendix A. Calculation of the zero-mode inverse localization length

The following subsections present exact analytical expressions for the zero-mode inverse localization length in the $\beta \rightarrow 0$ limit for $n = 3$, $n = 2$, and $n = 4$, respectively. The derivation for $n = 4$ (Appendix Appendix A.3) makes use of the intermediate result established in Appendix Appendix A.2.

Appendix A.1. Zero-mode inverse localization length for the $\beta \rightarrow 0$ limit with $n = 3$

For $\beta \rightarrow 0$ and $n = 3$, the inverse localization length of the zero-energy mode is

$$\nu = \left| \frac{1}{2\pi} \int_0^{2\pi} \ln |t_1 + \lambda \cos^3 x| dx \right|.$$

To evaluate this integral, we introduce the complex variable $z = e^{ix}$, for which

$$\cos x = \frac{1}{2} \left(z + \frac{1}{z} \right), \quad dx = \frac{dz}{iz}.$$

Using

$$\cos^3 x = \frac{1}{8} \left(z + \frac{1}{z} \right)^3,$$

we rewrite the integrand as

$$t_1 + \lambda \cos^3 x = \frac{1}{z^3} \left[\frac{\lambda}{8}(z^2 + 1)^3 + t_1 z^3 \right].$$

We therefore define the polynomial

$$P(z) = \frac{\lambda}{8}(z^2 + 1)^3 + t_1 z^3.$$

Since $|z| = 1$ on the integration contour, Jensen's formula gives

$$\frac{1}{2\pi} \int_0^{2\pi} \ln |t_1 + \lambda \cos^3 x| dx = \ln \left| \frac{\lambda}{8} \right| + \sum_{|z_j| > 1} \ln |z_j|,$$

where z_j are the six roots of $P(z) = 0$.

Next, we use the palindromic structure of $P(z)$. Dividing by z^3 , one obtains

$$\frac{P(z)}{z^3} = \frac{\lambda}{8} \left(z + \frac{1}{z} \right)^3 + t_1.$$

Introducing

$$w = z + \frac{1}{z},$$

the equation $P(z) = 0$ reduces to

$$\frac{\lambda}{8} w^3 + t_1 = 0, \quad \text{or} \quad w^3 = -\frac{8t_1}{\lambda}.$$

Let

$$s = \left(\frac{t_1}{\lambda} \right)^{1/3},$$

where the real cube root is taken for real t_1/λ . The three roots of the cubic equation can then be written as

$$w_0 = -2s, \quad w_1 = s(1 + i\sqrt{3}), \quad w_2 = s(1 - i\sqrt{3}).$$

For each w_μ , the corresponding z roots satisfy

$$z^2 - w_\mu z + 1 = 0.$$

Because the two roots always obey $z_+z_- = 1$, one root lies outside the unit circle and the other lies inside it, except at the transition point where they sit on the unit circle. Therefore, each w_μ contributes the logarithm of the modulus of the root with $|z| > 1$.

We first consider the real root $w_0 = -2s$. The corresponding quadratic equation is

$$z^2 + 2sz + 1 = 0.$$

For $|s| < 1$, both roots lie on the unit circle and hence give no contribution to the inverse localization length. For $|s| > 1$, the root outside the unit circle has modulus

$$|z| = |s| + \sqrt{s^2 - 1},$$

so that its contribution is

$$\delta_0 = \begin{cases} \ln \left(|s| + \sqrt{s^2 - 1} \right), & |s| > 1, \\ 0, & |s| < 1. \end{cases}$$

We next consider the complex-conjugate pair w_1 and w_2 . For each of them, the two roots of

$$z^2 - w_\mu z + 1 = 0$$

satisfy $z_+z_- = 1$, so that the contribution to Jensen's formula is given by the logarithm of the modulus of the root with $|z| > 1$. For the pair w_1 and w_2 , these contributions are equal and can be written compactly as

$$\delta_1 + \delta_2 = 2 \ln \left| \frac{w_1 + \sqrt{w_1^2 - 4}}{2} \right|,$$

where the branch of the square root is chosen continuously such that

$$\left| \frac{w_1 + \sqrt{w_1^2 - 4}}{2} \right| > 1.$$

Since $w_2 = \bar{w}_1$, the total contribution is manifestly real.

Collecting all contributions, we obtain the exact zero-mode inverse localization length in the form

$$\nu = \left| \ln \left| \frac{\lambda}{8} \right| + 2 \ln \left| \frac{w_1 + \sqrt{w_1^2 - 4}}{2} \right| + \delta_0 \right|,$$

with

$$w_1 = s(1 + i\sqrt{3}), \quad s = \left(\frac{t_1}{\lambda}\right)^{1/3}.$$

Equivalently, the result can be written explicitly as

$$\nu = \begin{cases} \left| \ln \left| \frac{\lambda}{8} \right| + 2 \ln \left| \frac{w_1 + \sqrt{w_1^2 - 4}}{2} \right| + \ln \left(|s| + \sqrt{s^2 - 1} \right) \right|, & |t_1/\lambda| > 1, \\ \left| \ln \left| \frac{\lambda}{8} \right| + 2 \ln \left| \frac{w_1 + \sqrt{w_1^2 - 4}}{2} \right| \right|, & 0 < |t_1/\lambda| < 1, \end{cases}$$

where the boundary case $|t_1/\lambda| = 1$ (i.e., $|s| = 1$) follows by continuity from either branch, since $\delta_0 = \ln(|s| + \sqrt{s^2 - 1}) \rightarrow 0$ as $|s| \rightarrow 1^+$. This representation is sufficient for determining the phase boundary from the condition $\nu = 0$ and can be evaluated numerically without ambiguity for all real t_1/λ .

As a consistency check, at the special point $t_1 = 0$ one has $s = 0$ and hence $w_1 = 0$. The above expression reduces to

$$\nu = \left| \ln \left| \frac{\lambda}{8} \right| \right|,$$

which agrees with the direct evaluation

$$\frac{1}{2\pi} \int_0^{2\pi} \ln |\lambda \cos^3 x| dx = \ln |\lambda| - 3 \ln 2 = \ln \left| \frac{\lambda}{8} \right|.$$

Therefore, the prefactor is fixed exactly by the analysis itself, and no additional fitting constant is needed.

Appendix A.2. Zero-mode inverse localization length for the $\beta \rightarrow 0$ limit with $n = 2$

For $\beta \rightarrow 0$ and $n = 2$, the inverse localization length of the zero-energy mode is

$$\nu = \left| \frac{1}{2\pi} \int_0^{2\pi} \ln |t_1 + \lambda \cos^2 x| dx \right|.$$

For $t_1 \neq 0$, the logarithmic integral can be written as

$$\frac{1}{2\pi} \int_0^{2\pi} \ln |t_1 + \lambda \cos^2 x| dx = \ln |t_1| + h\left(\frac{\lambda}{t_1}\right),$$

where

$$h(a) = \frac{1}{2\pi} \int_0^{2\pi} \ln |1 + a \cos^2 x| dx.$$

Using $\cos^2 x = (1 + \cos 2x)/2$, one obtains

$$1 + a \cos^2 x = A + B \cos 2x, \quad A = 1 + \frac{a}{2}, \quad B = \frac{a}{2}.$$

Since the average over $2x$ is equivalent to the average over one full period, $h(a)$ reduces to the standard integral [3, 58]

$$\frac{1}{2\pi} \int_0^{2\pi} \ln |A + B \cos \theta| d\theta = \begin{cases} \ln \left| \frac{A + \sqrt{A^2 - B^2}}{2} \right|, & A > |B|, \\ \ln \left| \frac{B}{2} \right|, & |A| < |B|. \end{cases}$$

Since $A^2 - B^2 = 1 + a$, the present parametrization gives $A > |B|$ for $a > -1$, whereas $|A| < |B|$ for $a < -1$. Therefore, for $a > -1$ one obtains

$$h(a) = \ln \left| \frac{1 + a/2 + \sqrt{1 + a}}{2} \right| = 2 \ln |1 + \sqrt{1 + a}| - \ln 4.$$

For $a < -1$, one obtains

$$h(a) = \ln \left| \frac{a}{4} \right|.$$

The two expressions coincide by continuity at $a = -1$. Therefore, the zero-mode inverse localization length is

$$\nu = \begin{cases} \left| 2 \ln \left| 1 + \sqrt{\frac{\lambda}{t_1} + 1} \right| + \ln |t_1| - \ln 4 \right|, & \lambda/t_1 > -1, \\ \left| \ln \left| \frac{\lambda}{4} \right| \right|, & \lambda/t_1 < -1. \end{cases}$$

For $t_1 = 0$, the result follows directly from

$$\frac{1}{2\pi} \int_0^{2\pi} \ln |\lambda \cos^2 x| dx = \ln |\lambda| - 2 \ln 2 = \ln \left| \frac{\lambda}{4} \right|.$$

Appendix A.3. Zero-mode inverse localization length for the $\beta \rightarrow 0$ limit with $n = 4$

For $\beta \rightarrow 0$ and $n = 4$, the inverse localization length of the zero-energy mode is

$$\nu = \left| \frac{1}{2\pi} \int_0^{2\pi} \ln |t_1 + \lambda \cos^4 x| dx \right|.$$

We evaluate the integral in different parameter regions.

For $\lambda/t_1 < -1$, namely $\kappa = \sqrt{-\lambda/t_1} > 1$, one may factorize the integrand as

$$1 + \frac{\lambda}{t_1} \cos^4 x = (1 + \kappa \cos^2 x) (1 - \kappa \cos^2 x).$$

The first factor $1 + \kappa \cos^2 x$ corresponds to the parameter value $a = \kappa > 0$, which falls in the $a > -1$ branch of Appendix [Appendix A.2](#). The second factor $1 - \kappa \cos^2 x$ corresponds to $a = -\kappa < -1$ (since $\kappa > 1$), which falls in the $a < -1$ branch. Applying the respective results from Appendix [Appendix A.2](#) to each factor and combining the two contributions, the zero-mode inverse localization length becomes

$$\begin{aligned} \nu &= \left| \frac{1}{2\pi} \int_0^{2\pi} \ln |1 + \kappa \cos^2 x| dx + \frac{1}{2\pi} \int_0^{2\pi} \ln |1 - \kappa \cos^2 x| dx + \ln |t_1| \right| \\ &= \left| [2 \ln |1 + \sqrt{1 + \kappa}| - \ln 4] + [\ln \kappa - \ln 4] + \ln |t_1| \right| \\ &= \left| 2 \ln |1 + \sqrt{1 + \kappa}| + \ln |\kappa| + \ln |t_1| - \ln 16 \right|. \end{aligned}$$

For $\lambda/t_1 > -1$, the zero-mode inverse localization length takes the form

$$\nu = \left| 2 \ln |1 + \sqrt{1 + \kappa}| + 2 \ln |1 + \sqrt{1 - \kappa}| + \ln |t_1| - \ln 16 \right|,$$

where $\kappa = (-\lambda/t_1)^{1/2}$. For $\lambda/t_1 < 0$, κ is real and positive. For $\lambda/t_1 > 0$, $\kappa = i|\kappa|$ is purely imaginary, so that $1 + \sqrt{1 - \kappa}$ and $1 + \sqrt{1 + \kappa}$ become complex; in this case the modulus $|\cdot|$ is taken before the logarithm, which ensures that ν remains real and non-negative for all parameter values. Throughout this appendix, the principal branch of the square root is used; the final expressions are understood through their absolute values, which makes the zero-mode inverse localization length single-valued and real.

Therefore, the zero-mode inverse localization length can be summarized as

$$\nu = \begin{cases} \left| 2 \ln |1 + \sqrt{1 + \kappa}| + 2 \ln |1 + \sqrt{1 - \kappa}| + \ln |t_1| - \ln 16 \right|, & \lambda/t_1 > -1, \\ \left| 2 \ln |1 + \sqrt{1 + \kappa}| + \ln |\kappa| + \ln |t_1| - \ln 16 \right|, & \lambda/t_1 < -1, \end{cases}$$

where in both cases $\kappa = (-\lambda/t_1)^{1/2}$, with the principal branch of the square root used throughout. The modulus $|\cdot|$ is taken before each logarithm to ensure that ν remains real and non-negative for all parameter values.

Data availability

The data that support the findings of this study are available from the corresponding author upon reasonable request.

Acknowledgments

Z. X. is supported by the NSFC (Grants No. 12375016 and No. 12461160324), Beijing National Laboratory for Condensed Matter Physics (Grant No. 2023BNL-CMPKF001). Y. N. is supported by the National Training Program of Innovation for Undergraduates (Grant No. 216972001).

References

- [1] I. C. Fulga, F. Hassler, A. R. Akhmerov, C. W. J. Beenakker, Scattering formula for the topological quantum number of a disordered multimode wire, *Phys. Rev. B* 83 (2011) 155429.
- [2] X. Cai, L. Lang, S. Chen, Y. Wang, Topological superconductor to anderson localization transition in one-dimensional incommensurate lattices, *Phys. Rev. Lett.* 110 (2013) 176403.
- [3] S. Longhi, Phase transitions in a non-hermitian aubry-andré-harper model, *Phys. Rev. B* 103 (2021) 054203.
- [4] A. Bansil, H. Lin, T. Das, Colloquium: Topological band theory, *Rev. Mod. Phys.* 88 (2016) 021004.

- [5] Z. Wang, Y. D. Chong, J. D. Joannopoulos, M. Soljačić, Reflection-free one-way edge modes in a gyromagnetic photonic crystal, *Phys. Rev. Lett.* 100 (2008) 013905.
- [6] Z. Wang, Y. D. Chong, J. D. Joannopoulos, M. Soljačić, Observation of unidirectional backscattering-immune topological electromagnetic states, *Nature* 461 (2009) 772–775.
- [7] A. Sinha, T. Shit, A. Tatarwal, D. Sen, S. Mukherjee, Probing the topological anderson transition in quasiperiodic photonic lattices via chiral displacement and wavelength tuning, *Phys. Rev. A* 112 (2025) 013512.
- [8] L. Lima, Interplay of phase transition from purely real and line-gapped phase on quantum entanglement in the generalized su–schrieffer–heeger model, *Phys. A Stat. Mech. Appl.* 694 (2026) 131574.
- [9] E. G. Cinnirella, A. Nava, G. Campagnano, D. Giuliano, Fate of high winding number topological phases in the disordered extended su-schrieffer-heeger model, *Phys. Rev. B* 109 (2024) 035114.
- [10] A. Nava, G. Campagnano, P. Sodano, D. Giuliano, Lindblad master equation approach to the topological phase transition in the disordered su-schrieffer-heeger model, *Phys. Rev. B* 107 (2023) 035113.
- [11] M. Scollon, M. P. Kennett, Persistence of chirality in the su-schrieffer-heeger model in the presence of on-site disorder, *Phys. Rev. B* 101 (2020) 144204.
- [12] Z. Lu, Y. Zhang, Z. Xu, Reentrant localization transitions in a topological anderson insulator: A study of a generalized su-schrieffer-heeger quasicrystal, *Front. Phys.* 20 (2025) 024204–.
- [13] Z. Lu, Z. Xu, Y. Zhang, Exact mobility edges and topological anderson insulating phase in a slowly varying quasiperiodic model, *Ann. Phys.* 534 (2022) 2200203.
- [14] L. Tang, S. Liu, G. Zhang, D. Zhang, Topological anderson insulators with different bulk states in quasiperiodic chains, *Phys. Rev. A* 105 (2022) 063327.

- [15] Z. Zuo, J. Lin, D. Kang, Topological inverse anderson insulator, *Phys. Rev. B* 110 (2024) 085157.
- [16] B. D. Assun ç ao, G. J. Ferreira, C. H. Lewenkopf, Phase transitions and scale invariance in topological anderson insulators, *Phys. Rev. B* 109 (2024) L201102.
- [17] C. Ouyang, Q. He, D. Xu, F. Liu, Higher-order topology in fibonacci quasicrystals, *Phys. Rev. B* 110 (2024) 075425.
- [18] G. Rai, H. Schlömer, C. Matsumura, S. Haas, A. Jagannathan, Bulk topological signatures of a quasicrystal, *Phys. Rev. B* 104 (2021) 184202.
- [19] A. Kobiałka, O. A. Awoga, M. Leijnse, T. Domański, P. Holmvall, A. M. Black-Schaffer, Topological superconductivity in fibonacci quasicrystals, *Phys. Rev. B* 110 (2024) 134508.
- [20] A. Sandberg, O. A. Awoga, A. M. Black-Schaffer, P. Holmvall, Josephson effect in a fibonacci quasicrystal, *Phys. Rev. B* 110 (2024) 104513.
- [21] R. Ji, Z. Xu, Fibonacci-modulation-induced multiple topological anderson insulators, *Commun. Phys.* 8 (2025) 336.
- [22] A. Padhan, S. R. Padhi, T. Mishra, Complete delocalization and reentrant topological transition in a non-hermitian quasiperiodic lattice, *Phys. Rev. B* 109 (2024) L020203.
- [23] S. Mansha, Y. D. Chong, Robust edge states in amorphous gyromagnetic photonic lattices, *Phys. Rev. B* 96 (2017) 121405.
- [24] C. Liu, W. Gao, B. Yang, S. Zhang, Disorder-induced topological state transition in photonic metamaterials, *Phys. Rev. Lett.* 119 (2017) 183901.
- [25] L. Lin, Y. Ke, C. Lee, Real-space representation of the winding number for a one-dimensional chiral-symmetric topological insulator, *Phys. Rev. B* 103 (2021) 224208.
- [26] G. Zhang, L. Tang, L. Zhang, D. Zhang, S. Zhu, Connecting topological anderson and mott insulators in disordered interacting fermionic systems, *Phys. Rev. B* 104 (2021) L161118.

- [27] J. Li, R. Chu, J. K. Jain, S. Shen, Topological anderson insulator, *Phys. Rev. Lett.* 102 (2009) 136806.
- [28] C. W. Groth, M. Wimmer, A. R. Akhmerov, J. Tworzydło, C. W. J. Beenakker, Theory of the topological anderson insulator, *Phys. Rev. Lett.* 103 (2009) 196805.
- [29] H. Jiang, L. Wang, Q. Sun, X. C. Xie, Numerical study of the topological anderson insulator in hgte/cdte quantum wells, *Phys. Rev. B* 80 (2009) 165316.
- [30] H. Liu, B. Xie, H. Wang, W. Liu, Z. Li, H. Cheng, J. Tian, Z. Liu, S. Chen, Acoustic spin-chern topological anderson insulators, *Phys. Rev. B* 108 (2023) L161410.
- [31] E. Meier, F. An, A. Dauphin, M. Maffei, P. Massignan, T. Hughes, B. Gadway, Observation of the topological anderson insulator in disordered atomic wires, *Science* 362 (2018) 929–933.
- [32] I. Mondragon-Shem, T. L. Hughes, J. Song, E. Prodan, Topological criticality in the chiral-symmetric aiii class at strong disorder, *Phys. Rev. Lett.* 113 (2014) 046802.
- [33] H. Zhang, A. Kamenev, Anatomy of topological anderson transitions, *Phys. Rev. B* 108 (2023) 224201.
- [34] Y. Xing, L. Zhang, J. Wang, Topological anderson insulator phenomena, *Phys. Rev. B* 84 (2011) 035110.
- [35] Y. Zhang, R. Chu, F. Zhang, S. Shen, Localization and mobility gap in the topological anderson insulator, *Phys. Rev. B* 85 (2012) 035107.
- [36] P. Titum, N. H. Lindner, M. C. Rechtsman, G. Refael, Disorder-induced floquet topological insulators, *Phys. Rev. Lett.* 114 (2015) 056801.
- [37] P. O. Christoph, S. Tibor, B. Christoph, L. S. Thomas, The topological anderson insulator phase in the kane-mele model, *Sci. Rep.* 6 (2016) 24007.
- [38] Z. Zhang, B. Wu, J. Song, H. Jiang, Topological anderson insulator in electric circuits, *Phys. Rev. B* 100 (2019) 184202.

- [39] P. Zhao, Z. Xiao, Y. Zhang, R. Shindou, Topological effect on the anderson transition in chiral symmetry classes, *Phys. Rev. Lett.* 133 (2024) 226601.
- [40] G. Liu, Y. Yang, X. Ren, H. Xue, X. Lin, Y. Hu, H. Sun, B. Peng, P. Zhou, Y. Chong, B. Zhang, Topological anderson insulator in disordered photonic crystals, *Phys. Rev. Lett.* 125 (2020) 133603.
- [41] Q. Lin, T. Li, L. Xiao, K. Wang, W. Yi, P. Xue, Observation of non-hermitian topological anderson insulator in quantum dynamics, *Nat. Commun.* 13 (2022) 3229.
- [42] C. Wang, T. Cheng, Z. Liu, F. Liu, H. Huang, Structural amorphization-induced topological order, *Phys. Rev. Lett.* 128 (2022) 056401.
- [43] X. Cui, R. Zhang, Z. Zhang, C. T. Chan, Photonic Z_2 topological anderson insulators, *Phys. Rev. Lett.* 129 (2022) 043902.
- [44] M. Ren, Y. Yu, B. Wu, X. Qi, Y. Wang, X. Yao, J. Ren, Z. Guo, H. Jiang, H. Chen, X.-J. Liu, Z. Chen, Y. Sun, Realization of gapped and ungapped photonic topological anderson insulators, *Phys. Rev. Lett.* 132 (2024) 066602.
- [45] A. Li, B. Xu, B. Xie, Successive phase transition in higher-order topological anderson insulators, *Phys. Rev. Res.* 7 (2025) 013204.
- [46] D. Bagrets, K. W. Kim, S. Barkhofen, S. De, J. Sperling, C. Silberhorn, A. Altland, T. Micklitz, Probing the topological anderson transition with quantum walks, *Phys. Rev. Res.* 3 (2021) 023183.
- [47] C. Grindall, A. C. Tyner, A.-K. Wu, T. L. Hughes, J. H. Pixley, Separate surface and bulk topological anderson localization transitions in disordered axion insulators, *Phys. Rev. Lett.* 135 (2025) 226601.
- [48] X. Li, H. Xu, J. Wang, L. Tang, D. Zhang, C. Yang, T. Su, C. Wang, Z. Mi, W. Sun, X. Liang, M. Chen, C. Li, Y. Zhang, K. Linghu, J. Han, W. Liu, Y. Feng, P. Liu, G. Xue, J. Zhang, Y. Jin, S. Zhu, H. Yu, S. P. Zhao, Q. Xue, Mapping the topology-localization phase diagram with quasiperiodic disorder using a programmable superconducting simulator, *Phys. Rev. Res.* 6 (2024) L042038.

- [49] S. Longhi, Topological anderson phase in quasi-periodic waveguide lattices, *Opt. Lett.* 45 (2020) 4036–4039.
- [50] Y. Deng, Y. He, Quadrupole moment of higher-order topological insulator at finite temperature, *Phys. Rev. B* 112 (2025) 205131.
- [51] A. K. Ghosh, T. Nag, A. Saha, Floquet second-order topological anderson insulator hosting corner localized modes, *Phys. Rev. B* 110 (2024) 125427.
- [52] Q. Dai, Z. Lu, Z. Xu, Emergence of multifractality through cascadelike transitions in a mosaic interpolating aubry-andré-fibonacci chain, *Phys. Rev. B* 108 (2023) 144207.
- [53] Y. Wang, G. Rai, C. Matsumura, A. Jagannathan, S. Haas, Superconductivity in the fibonacci chain, *Phys. Rev. B* 109 (2024) 214507.
- [54] M. Sbroscia, K. Viebahn, E. Carter, J. Yu, A. Gaunt, U. Schneider, Observing localization in a 2d quasicrystalline optical lattice, *Phys. Rev. Lett.* 125 (2020) 200604.
- [55] Y. Wang, W. You, Z. Xu, G. Sun, Generalized aubry-andré-harper model with power-law quasiperiodic potentials (2025). [arXiv:2511.13464](https://arxiv.org/abs/2511.13464).
- [56] H. Yao, T. Giamarchi, L. Sanchez-Palencia, Lieb-liniger bosons in a shallow quasiperiodic potential: Bose glass phase and fractal mott lobes, *Phys. Rev. Lett.* 125 (2020) 060401.
- [57] A. Jagannathan, The fibonacci quasicrystal: Case study of hidden dimensions and multifractality, *Rev. Mod. Phys.* 93 (2021) 045001.
- [58] S. Longhi, Metal-insulator phase transition in a non-hermitian aubry-andré-harper model, *Phys. Rev. B* 100 (2019) 125157.
- [59] A. Altland, D. Bagrets, L. Fritz, A. Kamenev, H. Schmiedt, Quantum criticality of quasi-one-dimensional topological anderson insulators, *Phys. Rev. Lett.* 112 (2014) 206602.
- [60] H. Liu, Z. Lu, X. Xia, Z. Xu, Fate of localization features in a one-dimensional non-hermitian flat-band lattice with quasiperiodic modulations, *New J. Phys.* 26 (9) (2024) 093007.